Earthquake Detectability and Depth Resolution with Dense Arrays in Long Beach, California: Further Evidence for Upper-Mantle Seismicity within a Continental Setting

A. Inbal[1], J.-P. Ampuero[2], R. Clayton[3]

Abstract

Dense array microearthquake detection and location is dependent on the array geometry and signal bandwidth. However, these dependencies have not been systematically characterized. Here, we quantify the resolution of the Long-Beach (LB) and the Extended Long-Beach (ELB) dense arrays, deployed along the Newport-Inglewood Fault (NIF), California. Previous study of the regional catalog and of downward-continued LB array data found NIF seismicity extending into the upper mantle beneath LB, but later studies, which analyzed the ELB raw data, found little evidence for such deep events. Here, the dense array discriminative power and depth resolution are characterized using pre-downward migrated LB seismograms and benchmark tests. An important factor controlling event detectability is the array-aperture-to-source-depth ratio. The LB array maximum aperture is only 20% larger than the ELB aperture, yet its resolution for deep (>20 km) events is improved by about a factor of two, suggesting that small changes to the array geometry may yield significant improvement to the resolution power. Assuming a constant aperture, we find the LB array maintain resolution with 1% of its sensors used for back-projection. However, the high sensor density is essential for improving the SNR. Analysis of the regional and array-derived NIF catalogs together with newly acquired Moho depths beneath the NIF, suggests mantle seismicity beneath LB is a robust feature of this fault.

Introduction

Seismicity occurring within urban environments poses a major hazard, but, characterizing the spatio-temporal distribution of earthquakes in urban areas is hindered by high levels of anthropogenic noise. For example, the Los Angeles (LA) basin, which is the densest population center in southern California, suffers from earthquake detectability that is far lower than in other, less-well instrumented regions. Dense array seismology, is well suited for signal detection in low

signal-to-noise-ratio (SNR) environments. This methodology utilizes finely sampled wavefields from closely-spaced seismometer- and smartphone-arrays [*Inbal et al.*, 2015, 2016, 2019; *Yang et al.*, 2021; *Yang and Clayton*, 2023], or fiber optic cables [*Zhan*, 2020; *Lellouch et al.*, 2021]. The main advantage of dense arrays over sparse networks is that the arrays may be used to detect events in data with poor signal-to-noise ratios (SNR), like the ones found in urban environments. Furthermore, array back-projection may be used to focus incoming signals onto the source region, thereby strongly facilitating their location.

The large data volume collected by dense observation systems requires the development of automatic processing tools, which sometimes involve complex source identification schemes. For simplicity, we assume here that the source discrimination scheme provides a binary outcome, meaning it accepts signals due to tectonic events and rejects all other signals, possibly assigning the detection some degree of likelihood. This step is routinely followed by phase association and source parameter determination. In reality, however, the discrimination and location stages are not independent, and since, except in a few places [e.g. *Yang and Clayton*, 2023], earthquake hypocenters generally occur below 2 km depth, the depth distribution can be used as a prior on the probabilistic discrimination stage. It is therefore convenient to use the inferred source depth (obtained for example via continuous back-projection imaging) as an additional check in the discrimination procedure, together with the signal's temporal and spectral properties. However, it is not clear whether dense arrays, which are often deployed in noisy environments, and whose aperture do not exceed a few km, possess sufficient resolution power at seismogenic depths.

We restrict our analysis to geometries in which the potential source lies beneath the array, a situation common in dense array studies [e.g. *Inbal et al.*, 2016; *Peña Castro et al.*, 2019; *Catchings et al.*, 2020; *Yang et al.*, 2021, 2022; *Yang and Clayton*, 2023]. To investigate dense

array source detectability and depth resolution, we consider the Long Beach (LB ; 5200 sensors ; deployed between January to June, 2011) and the Extended Long Beach (ELB ; 2500 sensors ; deployed between January to March, 2012) array datasets. The two arrays were located along adjacent portions of the Newport-Inglewood Fault (NIF), a major fault traversing the LA basin (Figure 1). *Inbal et al.* [2015, 2016, hereafter referred to as I2016 and I2015, respectively] used the LB dataset to compile a catalog for the portion of the NIF in LB, by enhancing the event detectability via sub-array stacking and downward-continuation [*Gazdag*, 1978]. This allowed them to detect abundant seismicity occurring in the lower crust and upper mantle. The depth range was unusual given that, except for a few places, seismicity in southern California is generally confined to the upper 12 km or so [e.g. *Hauksson*, 2011]. Thus, I2016's findings challenged the common understanding regarding the physical mechanisms allowing faulting at depth. Recently, *Yang et al.* [2021, hereafter referred to as Y2021] introduced a new detection scheme which relies on the SNR of the back-projected surface data before and after trace randomization, and applied it to the ELB dataset. They identified a small number of deep NIF earthquakes, confirming I2015's and I2016's finding that the detection of deep events requires pre-processing the dense array data prior to back-projection. Here, we assess the discriminative power and depth resolution of dense arrays by using seismograms of deep NIF earthquakes and a set of synthetic tests. In light of these results, we reexamine the NIF seismic catalogs along with newly acquired Moho depths in the LB area [*Clayton*, 2020], and confirm the results of I2015 and I2016.

Observing Deep Earthquakes on the LB array

Dense array analysis enhances the SNR by beamforming (i.e. delay-and-sum) the array's seismograms. Assuming the noise recorded by the array is uncorrelated between the array's sensors, this procedure improves the SNR by a factor proportional to $\sqrt{N}$, where N is the number

of sensors in the array [e.g. *Rost and Thomas*, 2002]. If the target area lies beneath the array, and if a detailed velocity model is available, then further SNR improvement can be obtained by wavefield extrapolation using downward-continuation [*Gazdag*, 1978], which enhances near-vertical signals impinging on the array. We discuss the improvement in source-depth resolution due to downward-continuation in the section Spatial Resolution Analysis.

Because the seismic source spectral and temporal properties generally differ from the properties of signals due to man-made sources, it is possible to distinguish between tectonic and non-tectonic signals from the statistical properties of the time series of back-projected images. I2015 and I2016 analyzed the properties of source images obtained by continuously back-projecting envelopes of the downward-continued LB array dataset. They found that the statistical distribution of the images containing newly identified tectonic sources was significantly different from the one associated with images of non-tectonic sources. The former follows a power-law distribution, while the latter follows a Gumbel distribution. I2015 and I2016 declared a detection if the maximum amplitude of the BP image exceeded 5 times the Median Absolute Deviation (MAD) of the amplitude of the BP images around the detection time. Using this detection threshold and the cumulative probabilities of the signal and noise BP images, I2015 found the false detection rate to be 2×10^{-3} per night.

Y2021 took a different approach for discriminating coherent seismic sources from noise sources in dense array recordings, which they refer to as Trace Randomization (TR). To test for the presence of a tectonic signal, the TR scheme spatially redistributes envelopes of the array seismograms by assigning them random positions within the array. The TR-detection criteria is based on the degree of back-projected energy reduction due to the randomization, derived from

the ratio between the pre- and post-randomized maximal back-projected energy amplitudes as:

$$R = 1 - \frac{E^{post}}{E^{pre}}, \tag{1}$$

where E^{pre} and E^{post} are the pre- and post-TR maximal energy levels, respectively. Neglecting random uncorrelated noise fields which occasionally give rise to $E^{post} > E^{pre}$, Y2021 proposed an R-based detection criteria, applied to windows with $E^{pre} > 5 \times MAD(E^{pre})$ around the detection time. According to the R-based detection scheme, uncorrelated noise sources should exhibit $R \sim 0$, while coherent tectonic sources should exhibit $R \sim 1$. Thus, the statistical properties of a distribution of R-values computed over multiple time windows, would allow one to discriminate between deep, temporally-isolated coherent sources to shallow uncorrelated noise sources common in continuous urban dense array data.

Given that Y2021 found only a few deep NIF earthquakes, it is instructive to characterize the LB and ELB array's capacity for detecting small-magnitude events in the pre-downward continued data. We do that by employing the TR scheme on LB array data containing signals from deep earthquakes occurring along the NIF. Many of the NIF earthquakes, which are located directly beneath the LB and ELB arrays, exhibit poor surface SNR. To enable their detection, I2015 and I2016 applied sub-array stacking and downward-continuation, which significantly improved the SNR. Some of the events, however, may be identified on the filtered pre-downward-continued array data. An example is shown in Figure 2, which presents LB array data containing 5 earthquakes recorded during March 2011, whose magnitudes were between 0 to 0.2, and whose focal depths were found to lie between 15 to 20 km. The top row shows the amplitudes of ground-velocity envelopes, computed by filtering the seismograms between 2 to 10 Hz, squaring, and smoothing using a 0.1 s running median window. The traces are ordered with respect to the

hypocentral distance obtained by I2016. For each trace we compute the P-wave train SNR by taking the ratio between the mean energy in a 0.8 s window around the P-wave arrival to the mean in the 4 s preceding the event. Panels a to e show the amplitudes for traces with SNR>1, totaling about 40% of the array's recordings. The seismic arrivals are clearly observed between 33 to 38 s in each of the record sections. The panels on the bottom row in Figure 2 show the distribution of the SNR as a function of the sensor location. Note that in a few cases (e.g. panel f and i), the epicenter is located near a cluster of high SNR traces. However, due to LB urban noise levels, the surface detection pattern is generally not well correlated with the epicentral location, which complicates the detection procedure. We used the relation in Equation 1 to compute the R-values for the time windows containing the arrivals in the seismograms shown in Figure 2a-e, and found that R varies between 0.01 to 0.2 for these five events. These R-values are lower than the threshold of Y2021 for the ELB dataset, which was set to 0.2735.

Synthetic Tests for Characterizing the Effects of the Signal-to-Noise Ratio and Array Aperture on Source Discrimination

To examine why the LB back-projection energy reduction may sometime tend to 1 (i.e. $R = 0$) for seismograms containing tectonic signals correlated among 40% of the array's sensors, and to assess how the R-values are influenced by the array's aperture and SNR levels, we applied a series of tests using two synthetic datasets. In the first set of tests, we generate synthetic seismograms assuming a population of sources whose numbers exponentially decay with depth, similar to the source depth distribution in the LB catalog compiled by I2016. For each source, we compute R^{ELB} and R^{LB} for a monochromatic 5-Hz input signal modulated by an envelope whose amplitude decays exponentially with time over a time scale of a few seconds, and which propagates in a uniform velocity model. The spectral content of the synthetic signal is selected

based on NIF earthquake seismograms analyzed by I2015 and I2016. We add white noise to the seismograms such that their SNR is smaller than one, similar to urban dense-array datasets. In the second set of tests, we compute R using traces containing uncorrelated random noise. The results are presented in Figure 3. The blue curve in panel a shows the value of R^{ELB} as a function of source depth. Note that R-values are depth-dependent, such that larger values are systematically associated with sources at shallow depths, which implies that an R-based detector may miss deep seismic events. This depth bias is only slightly reduced by increasing the aperture of the array, as shown by the red curve in Figure 3a, which indicates R^{LB} values as a function of source depth. Note that, since $R^{LB} > R^{ELB}$, the TR-based detection statistics obtained for the ELB geometry by Y2021 do not apply straightforwardly to the LB array geometry. Also, the value of R computed for the March 2011 earthquakes shown in Figure 2 is considerably smaller than the synthetic value, which likely reflects the poor SNR conditions (i.e. array-averaged SNR) of the LB array data. However, this does not effect the trend with depth shown in Figure 3a.

The results presented in Figure 3 provide further insights on the importance of the array aperture for source discrimination. That discrimination scheme is most effective for sources associated with a large scatter of the inter-array time delays, a requirement that is met when the array aperture is close to or larger than the source depth. When the aperture-to-source-depth ratio is large, TR is expected to significantly decrease E^{post} relative to E^{pre}, thereby providing a reliable detection statistic. For the LB and ELB arrays, this condition applies to events occurring above approximately 8 km and 12 km, respectively. On the other hand, when the aperture-to-source-depth ratio is much smaller than one, the range of inter-array time delays ("normal moveout") tends to zero, thereby reducing the discriminative power of the array. The discriminative power can be parametrized by the array's time-delay Median Absolute Deviation

(MAD$_{\Delta t}$), the value of which is dependent on the array aperture and source depth, as well as on the SNR and the time delay resolution. In general, MAD$_{\Delta t}$ decreases with source depth, with faster decrease rates for small-aperture arrays (Figure 4). Thus, for very small arrays or very deep sources, we expect MAD$_{\Delta t} \rightarrow 0$. The narrow range of time-delays obtained in these situations is expected to yield R-values close to zero, and therefore cause the detector to miss some weak events.

The array's discriminative power is also affected by the SNR. For poor-SNR signals, the ratio E^{post}/E^{pre} can occasionally be significantly smaller than one, which may result in a false detection. To illustrate this effect, we indicate in Figure 3 the R^{ELB}-value reported by Y2021, and the one obtained in this study by the dashed and yellow vertical lines, respectively. Note that Y2021's R^{ELB}-value was computed using thousands of time windows passing their initial detection criteria, whereas the R^{ELB} reported here is a depth-averaged value computed using only windows containing a coherent synthetic source, yet the two values closely match. Since most of the windows Y2021 used for computing R^{ELB} likely do not contain a tectonic signal, this result suggests the R-based scheme may not be suitable for discriminating deep sources. We find this issue repeats when the approach is applied to data containing random uncorrelated noise. For this type of input, the fluctuations around the mean value of R can be quite large, and are generally dependent on factors such as the sampling interval and the envelope calculation method. For the commonly used nth-root stacking [e.g. *Rost and Thomas*, 2002, with n=3], the average value of R is close to 0, as expected for records containing only uncorrelated random noise. However, after neglecting cases in which $R < 0$, we find that 34% the windows have $0 < R < 0.3$ and 13% of the windows have $0.3 < R < 0.6$ (see dark and light-grey rectangles in panel 3a), within the range of results from tests containing a coherent source (blue curve in Figure 3a). In fact, the

range of depths allowing for reliable source discrimination on the pre-downward migrated ELB array is limited to the upper 8 km, since the statistics for deeper sources are not significantly different from the ones associated with a random noise field.

Thus far, we have estimated the detection sensitivity to the array aperture and SNR. Next, we estimate the source depth error by comparing the source depth obtained from back-projecting the LB signal envelopes to the input source depth, after adding white uncorrelated noise. The noise amplitude is uniformly distributed over the range between -0.8 to 0.8 times the maximum envelope amplitude. The results are presented in Figure 3b, which shows the distribution of source depth discrepancies. We find that the source depth error is about 2 km, consistent with the results of synthetic tests presented by I2016. In addition, for the range of source-aperture-to-source-depth ratios examined here, we do not find that the depth error correlates with the source depth. This suggests that the dominant factor limiting accurate source depth determination is the array aperture, assuming the sources lie within the array's footprint, and that their signals exceed the noise level. Thus, resolving the depth of earthquakes occurring beneath the array may be obtained by a subset of the array's sensors, given that (1) the source-depth-to-array-aperture ratio is smaller than about 2, and (2) the SNR is larger than 1. We test the validity of this statement by using synthetic tests presented in the next section.

Spatial Resolution Analysis

We estimate the source imaging resolution using Point Spread Functions (PSF), which describe the effect of the imaging system on the imaged object [e.g. *Lecomte et al.*, 2015; *Nakahara and Haney*, 2015]. The degree of source resolution and illumination may be derived from basic principles of ray theory, by considering the density of source-to-array raypaths. In this framework, a well illuminated source is defined as one for which ray paths cover a large fraction of the focal

sphere. In an isotropic medium, the wavenumber vector is at any point perpendicular to the wavefront, and thus its orientation and amplitude in the source region may be used to determine the source image spatial resolution. For a source at location j imaged by a station at location i, the local wavenumber vector is defined by the projection of the source Fourier components onto the local slowness vector [*Lecomte et al.*, 2015]:

$$k_{ij}^{local} = \omega \cdot S_{ij}, \tag{2}$$

where ω represents the angular frequency, and S_{ij} is the local slowness vector, which is parallel to the ray connecting the j'th source with the i'th station. In practice, each frequency component is weighted by the source spectra, and as a result, wideband sources are expected to be better resolved than narrowband sources. The spatial resolution is also dependent on the aperture of the array. Increasing the array aperture will increase the local wavenumber density, which improves the illumination and enhances the imaging resolution. The PSF is obtained from k^{local} after weighting by the source spectra by summing over available source-to-array ray paths, and then taking the inverse spatial Fourier transform. The advantage of this approach is that it allows us to compute PSFs that are independent of the noise, and ensures that the spatial variability of urban noise levels [*Riahi and Gerstoft*, 2015; *Inbal et al.*, 2019] does not effect the resolution estimates.

To quantify the spatial resolution and analyze its dependency on the source depth, we compute the PSF for the LB and ELB array geometries. As input, we use the spectra of the envelope of the 5 Hz exponentially decaying sine function discussed in the previous section. Equation 2 is solved assuming a uniform velocity model of 3.5 km/s, neglecting the effects of scattering on the PSF [*Lecomte et al.*, 2015]. Figure 5 presents the spatial resolution for shallow (10 km;

panels a,b) and deep (20 km; panels c,d) sources. In the absence of noise in the input data and velocity model, the only effect reducing the source depth resolution is the limited aperture of the array, which is manifested by the smearing of the PSFs along the depth axis. This affects the ELB and LB array differently, and is most noticeable for sources located below 12 km, for which the vertical resolution of the ELB degrades rapidly with depth. To illustrate this effect, we present in Figure 5e the vertical resolution scale, defined as the vertical extent over which the PSF value decreases down to 80% relative to the maximum PSF value at the focal point. For shallow sources (< 10 km), both arrays can well resolve sources located less than 1 km apart. However, the limited aperture of the ELB array yields images whose resolution power at large depths is reduced relative to the LB array. Events located at depths larger than about 20 km are not well resolved by the ELB array, but may be resolved by the LB array. This effect is an outcome of a modestly wider aperture (both in the NS and in the EW direction ; see Figure 1) of the LB array relative to the ELB array.

We also investigated the effects of downward-continuation [*Gazdag*, 1978] of the wavefield on the vertical resolution. Reducing the vertical separation by wavefield extrapolation has the desired effect of increasing the $\mathrm{MAD}_{\Delta t}$. The direct consequence is a significant increase in the vertical resolution scale. This is illustrated by the dashed curve in Figure 5e, showing the vertical resolution for the LB array after wavefield extrapolation down to 5 km depth. For the deepest events located below 25 km, downward continuation may improve the vertical resolution by as much as 40%. Note that these estimates provide a lower bound on the improvement in the resolution. The SNR may be improved prior to conducting downward continuation by applying plain-stack (i.e. setting the array's time delays equal to zero) of small sub-arrays within the LB array, which tends to de-amplify surface waves generated by shallow sources. Additionally,

downward continuation further de-amplifies such arrivals, and is thus expected to improve the vertical resolution relative to what is shown in Figure 5e.

Recent studies suggest the dramatic increase in the spatial sampling of the seismic wavefield provided by state-of-the-art seismic imaging systems may help improve earthquake detectability and hence refine existing catalogs [*Inbal et al.*, 2019; *Lellouch et al.*, 2021; *Mesimeri et al.*, 2021; *Arrowsmith et al.*, 2022]. For example, *Inbal et al.* [2019] evaluated the earthquake location accuracy achieved by dense noisy smartphone arrays. They found that back-projecting only 0.5% of the available smartphone-derived seismograms in the LA area would allow detection of events with M$\sim$1, approximately one magnitude unit below the catalog magnitude of completeness in that region. This smartphone-user density was required in order to enhance the SNR of smartphone-recorded signals due to M$\sim$1 earthquakes. However, it is not clear what is the minimum density required in order to resolve the location of back-projected signals that standout of the noise level.

Next, we use a bootstrap analysis to assess the sensitivity of location estimates of signals with SNR>1 to the density of the array. To do that, we compute the PSF for the LB configuration by using only 1% of the available LB sensor positions, which we refer to as the sparse array configuration. For each input source depth value, we generate 100 sparse configurations randomly selected from the LB array sensor locations. The results are presented in Figure 5e, which shows the average resolution of the vertical location of the source for the sparse array dataset. Remarkably, we find that the sparse configuration is almost as effective as the dense configuration for resolving earthquake-like signals with SNR>1 located beneath the array. Moreover, we find that the resolution on deep (>15 km) sources obtained by using the sparse configuration exceeds the resolution of the 2500-sensors ELB array for sources lying at this depth range. Thus, an array

whose dimensions are comparable to the LB array, but which contains only a small number of sensors, can be used to locate signals excited by deep tectonic events if they exceed the ambient noise level, and occur within the array's footprint. The logic also applies to the local seismic network operating in the LA area, whose inter-sensor distances are of the order of 10 km. Back-projecting signals recorded by this network onto the NIF fault may help obtain robust locations, and reduce the local catalog's magnitude of completeness [*Inbal et al.*, 2023].

Implications for the Resolution of Deep (>20 km) Seismicity beneath the Long Beach the Extended Long Beach Arrays

The distribution of seismicity along the NIF obtained from the LB and ELB arrays, and from the regional network, together with newly acquired Moho depths [*Clayton*, 2020] are shown in Figure 6. As was previously suggested by I2015 and I2016, many of the events in the LB section of the NIF occur in the lower crust, and some events occur in the upper mantle (Figure 6a). The frequency-magnitude distribution in the LB back-projection-based catalog is complete down to about $M = -1$. After adjusting for the area and time-window of the LB deployment, the distribution nicely extrapolates to the one of seismicity in the regional catalog, which is complete above M$\sim$2 [*Inbal et al.*, 2015]. Thus, we think the LB distribution reflects the long-term behavior of the NIF, rather than some transient behavior. We note that the focal depth distribution is observed for hypocenters whose arrivals were detected via match-filter analysis of regional records [*Ross et al.*, 2019], which further supports our observations. Accounting for the combined uncertainty on the Moho and source depths suggests the deepest events are well within the upper mantle.

An adjacent cross-section located below the ELB array is shown in Figure 6b. The focal depth distribution for the ELB section is skewed towards depth larger than 10 km, in disagreement

with the distribution of Y2021, which mostly consists of events occurring in the upper 10 km. Although it does not contain mantle earthquakes, the ELB maximum focal depths are larger than the ones observed along seismically active fault sections cutting through thin-crustal zones in southern California.

Summary

We examine the depth resolution of dense seismic arrays for sources lying beneath the array. We find that the parameter controlling the resolution power is the source-depth-to-array-aperture ratio and the source's bandwidth. The source-array geometry effect on the resolution can be parameterized by the MAD of the inter-array time delay distribution, which is sensitive to modest changes in the aperture. The LB array maximum aperture is only 20% larger than the ELB array maximum aperture, yet its source depth resolution for deep (>20 km) events is improved by about a factor of two (Figure 3), which indicates that small changes to the array geometry may yield significant improvement to the resolution power. In addition, we find that using only 1% of the LB array sensors does not significantly affect the depth resolution of signals with SNR>1, given the sensor subset maintains an aperture close to aperture of the entire array.

We use synthetic tests to evaluate the performance of the TR -based approach of Y2021. We find that this scheme is sensitive to the array aperture, and is expected to detect more shallow-depth events than deep events. This sensitivity also suggests the results obtained by Y2021 for the ELB dataset may not straightforwardly apply to the LB dataset. In addition, the TR-based scheme may sometimes classify a random noise field as a tectonic signal. This is demonstrated in the following manner: if we assume the input source depths are exponentially distributed and truncated below 35 km, and that all time windows contain arrivals from no more than a single

earthquake, then we find the mean R^{ELB}-value equal to 0.278 (dashed curve in panel 3b). This value is almost identical the R^{ELB} value computed by Y2021 for noise-dominated time windows.

The factors promoting earthquake nucleation below the seismogenic zone remain poorly resolved. Earthquakes are the result of stick-slip frictional instabilities that occur due to brittle fracture of rock, a behavior that is strongly dependent on the ambient pressure-temperature, lithology, strain rate, and pore pressure. In southern California, the maximum depth of seismicity largely coincides with the 400°C isotherm [*Bonner et al.*, 2003; *Hauksson*, 2011]. That correlation is thought to manifest thermal effects on the rheology, with the deep termination of seismicity corresponding to the onset of plastic yielding in Quartz-rich rocks [e.g. *Scholz*, 2002]. Clusters of deep events are common in thick-crustal, rapidly-deforming regions, where the local isotherm is depressed downwards due to lower-than-average heat-flow [*Bonner et al.*, 2003], or where faults cut through mafic lithology [*Magistrale and Sanders*, 1996; *Magistrale*, 2002], which tend to exhibit brittle behavior at larger depths. The NIF events are an exception to this rule. They represent some of the deepest earthquakes in California, yet they occur on slowly deforming faults cutting through the thinnest crust in California, whose associated heat flow is close to the regional average. Thus, the width of the seismogenic zone along the NIF challenges our understanding of the processes responsible for earthquake rupture. Since the maximum earthquake magnitude for a given fault is a function of its width, the seismicity depth extent also bears strong implications for seismic hazard in the LA urban area.

Data and Resources. The Southern California Earthquake Data Center earthquake catalog is available at the following doi: `https://scedc.caltech.edu`. The LB seismicity catalog is from *Inbal et al.* [2016], and the ELB seismicity catalog is from *Yang et al.* [2021].

Acknowledgments. We thank L. Yang for providing the ELB seismicity catalog used in their study. The authors acknowledge there are no conflicts of interest recorded.

References

Arrowsmith, S. J., D. T. Trugman, J. MacCarthy, K. J. Bergen, D. Lumley, and M. B. Magnani (2022), Big Data Seismology, *Rev. Geophys.*, *60*(2), e2021RG000,769, doi:https://doi.org/10.1029/2021RG000769.

Bonner, J. L., D. D. Blackwell, and E. T. Herrin (2003), Thermal Constraints on Earthquake Depths in California, *Bull. Seis. Soc. Am.*, *93*(6), 2333–2354, doi:10.1785/0120030041.

Catchings, R. D., M. R. Goldman, J. H. Steidl, J. H. Chan, A. A. Allam, C. J. Criley, Z. Ma, D. S. Langermann, G. J. Huddleston, A. T. McEvilly, D. D. Mongovin, E. M. Berg, and Y. Ben-Zion (2020), Nodal Seismograph Recordings of the 2019 Ridgecrest Earthquake Sequence, *Seismo. Res. Lett.*, *91*(6), 3622–3633, doi:10.1785/0220200203.

Clayton, R. W. (2020), A detailed image of the continent-borderland transition beneath Long Beach, California, *Geophys. J. Int.*, *222*(3), 2102–2107, doi:10.1093/gji/ggaa286.

Gazdag, J. (1978), Wave equation migration with the phase-shift method, *Geophysics*, *13*(7).

Hauksson, E. (2011), Crustal geophysics and seismicity in southern California, *Geophys. J. Int.*, *186*(1), 82–98, doi:10.1111/j.1365-246X.2011.05042.x.

Inbal, A., R. W. Clayton, and J.-P. Ampuero (2015), Imaging widespread seismicity at midlower crustal depths beneath Long Beach, CA, with a dense seismic array: Evidence for a depth-dependent earthquake size distribution, *Geophys. Res. Lett.*, *42*(15), 6314–6323, doi:10.1002/2015GL064942.

Inbal, A., J.-P. Ampuero, and R. W. Clayton (2016), Localized seismic deformation in the upper mantle revealed by dense seismic arrays., *Science*, *354*(6308), 88–92, doi:10.1126/science.aaf1370.

Inbal, A., Q. Kong, W. Savran, and R. M. Allen (2019), On the Feasibility of Using the Dense MyShake Smartphone Array for Earthquake Location, *Seismo. Res. Lett.*, doi:10.1785/0220180349.

Inbal, A., T. Cristea-platon, J.-p. Ampuero, G. Hillers, and D. Agnew (2023), Reply to Comment on ‘ Sources of Long-Range Anthropogenic Noise in Southern California and Implications for Tectonic Tremor Gregor Hillers , Duncan Agnew , and Susan E . Hough ” by Allie, *Bull. Seismo. Soc. Am.*, pp. 1–15, doi:10.1785/0120200007.

Lecomte, I., P. Lubrano-Lavadera, A. Wuestefeld, T. Kaschwich, J. Albaric, and H. N. Gharti (2015), Focusing in migration-based location of weak microseismicity: modelling point-spread function for resolution analyses, in *SEG Technical Program Expanded Abstracts 2015*, pp. 2491–2495, Society of Exploration Geophysicists, doi:10.1190/segam2015-5813282.1.

Lellouch, A., R. Schultz, N. Lindsey, B. Biondi, and W. Ellsworth (2021), Low-Magnitude Seismicity With a Downhole Distributed Acoustic Sensing Array—Examples From the FORGE Geothermal Experiment, *J. Geophys. Res.*, *126*(1), e2020JB020,462, doi:10.1029/2020JB020462.

Magistrale, H. (2002), Relative contributions of crustal temperature and composition to controlling the depth of earthquakes in Southern California, *Geophys. Res. Lett.*, *29*(10), 87–1–87–4, doi:10.1029/2001GL014375.

Magistrale, H., and C. Sanders (1996), Evidence from precise earthquake hypocenters for segmentation of the San Andreas Fault in San Gorgonio Pass, *J. Geophys. Res.*, *101*(B2), 3031–3044,

379 doi:10.1029/95JB03447.

380 Mesimeri, M., K. L. Pankow, and J. Rutledge (2021), A Frequency-Domain-Based Algorithm
381 for Detecting Microseismicity Using Dense Surface Seismic Arrays, *Bull. Seismo. Soc. Am.*,
382 *111*(5), 2814–2824, doi:10.1785/0120210062.

383 Nakahara, H., and M. M. Haney (2015), Point spread functions for earthquake source imaging:
384 an interpretation based on seismic interferometry, *Geophys. J. Int.*, *202*(1), 54–61, doi:10.
385 1093/gji/ggv109.

386 Peña Castro, A. F., S. L. Dougherty, R. M. Harrington, and E. S. Cochran (2019), Delayed
387 Dynamic Triggering of Disposal-Induced Earthquakes Observed by a Dense Array in Northern
388 Oklahoma, *J. Geophys. Res.*, *124*(4), 3766–3781, doi:10.1029/2018JB017150.

389 Riahi, N., and P. Gerstoft (2015), The seismic traffic footprint: Tracking trains, aircraft, and
390 cars seismically, *Geophys. Res. Lett.*, *42*(8), 2674–2681, doi:10.1002/2015GL063558.

391 Ross, Z. E., D. T. Trugman, E. Hauksson, and P. M. Shearer (2019), Searching for hidden earth-
392 quakes in Southern California., *Science*, *364*(6442), 767–771, doi:10.1126/science.aaw6888.

393 Rost, S., and C. Thomas (2002), Array seismology: Methods and applications, *Reviews of Geo-*
394 *physics*, *40*(3), 1008, doi:10.1029/2000RG000100.

395 Scholz, C. (2002), *The Mechanics of Earthquakes and Faulting*, Cambridge University Press.

396 Yang, L., X. Liu, and G. C. Beroza (2021), Revisiting evidence for widespread seismicity in the
397 upper mantle under Los Angeles., *Science Adv.*, *7*(4), eabf2862, doi:10.1126/sciadv.abf2862.

398 Yang, L., X. Liu, W. Zhu, L. Zhao, and G. C. Beroza (2022), Toward improved urban earthquake
399 monitoring through deep-learning-based noise suppression, *Science Adv.*, *8*(15), eabl3564, doi:
400 10.1126/sciadv.abl3564.

401 Yang, Y., and R. W. Clayton (2023), Shallow Seismicity in the Long Beach–Seal Beach, California
402 Area, *Seismo. Res. Lett.*, *94*(4), 1948–1956, doi:10.1785/0220220358.
403 Zhan, Z. (2020), Distributed Acoustic Sensing Turns Fiber-Optic Cables into Sensitive Seismic
404 Antennas, *Seismo. Res. Lett.*, *91*(1), 1–15, doi:10.1785/0220190112.

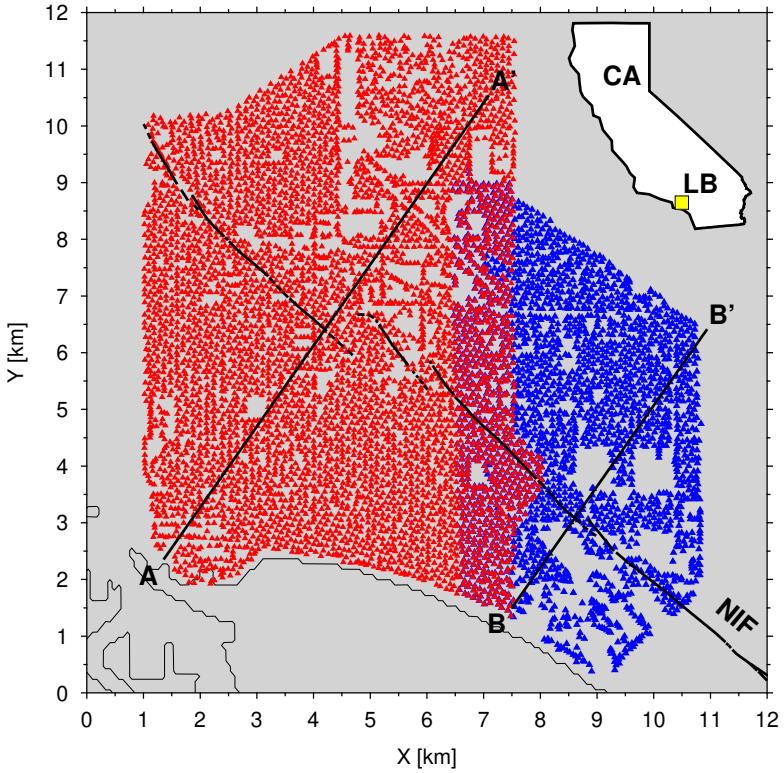

Figure 1. Location map. Red and blue triangles indicate the locations of the LB and ELB array sensors, respectively. The thick black line shows the location of the Newport-Inglewood Fault. Lines A-A' and B-B' refer to depth cross-sections shown in Figure 6. Thin black line marks the coastline. Inset map shows the location of Long Beach within the state of California. Abbreviations: NIF: Newport-Inglewood Fault, LB: Long Beach, CA: California.

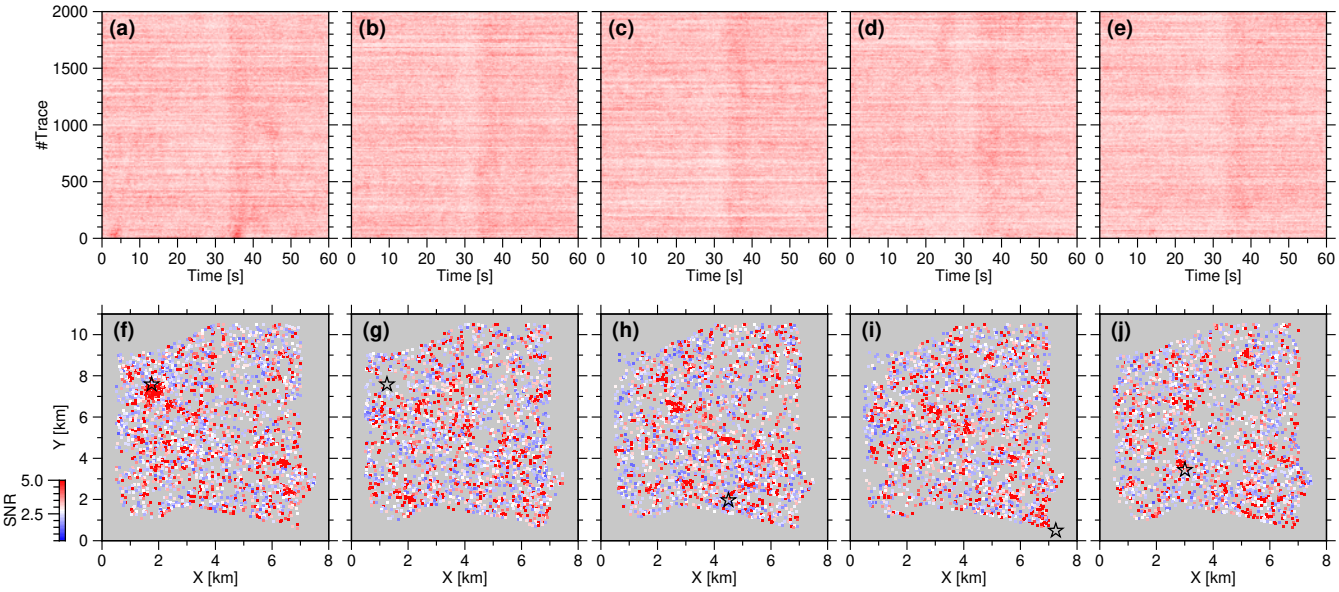

Figure 2. Seismograms recording arrivals from earthquakes occurring during March 2011 beneath the LB array. Top row shows the 2 to 10 Hz envelope amplitudes as a function of time for 2000 traces with SNR>1. Bottom row shows the distribution of the maximal amplitudes relative to the pre-event noise as a function of location. The star indicates the epicentral location. Day of detection, magnitude and depth are as follows: a,f March 16, 2011, M0.1, 17 km ; b,g March 18, 2011, M0.1, 17 km ; c,h March 8, 2011, M0.06, 16 km ; d,i March 15, 2011, M0.2, 16 km ; e,j March 5, 2011, M0.07, 19 km.

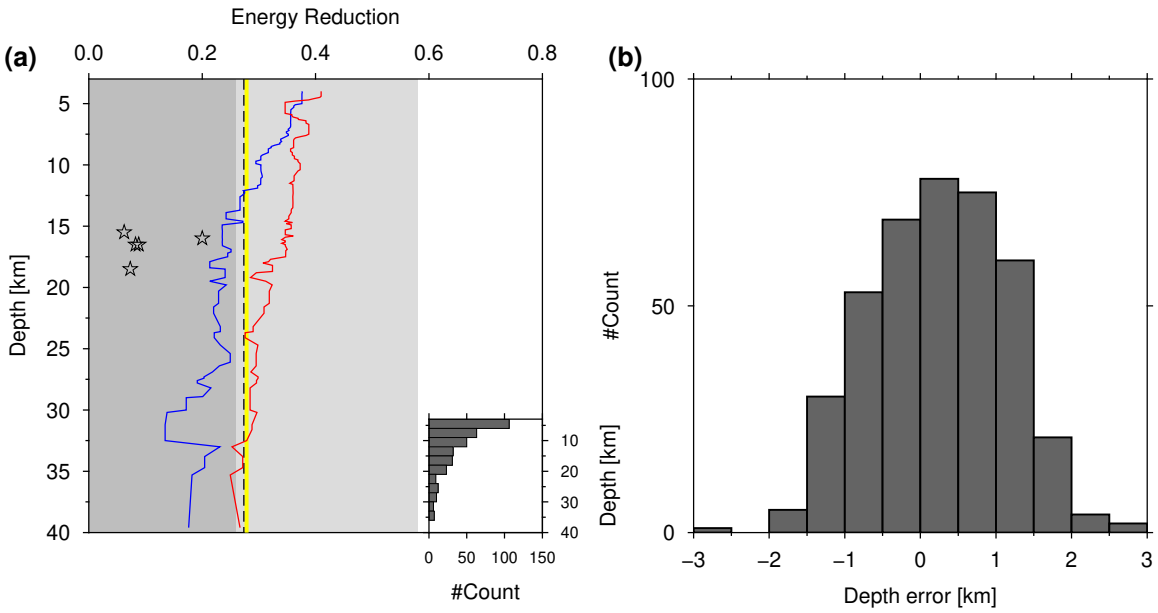

Figure 3. Synthetic tests for source discrimination using Trace Randomization. a. The back-projected energy reduction as a function of the input source depth. Solid lines indicate the level of energy reduction (defined in Equation 1), for synthetic tests in which the input source depths are exponentially distributed (as in the inset histogram), with blue and red colors for the ELB and LB array, respectively. Dashed vertical line indicates the mean back-projected energy reduction for the ELB data reported by *Yang et al.,* 2021, and the yellow line indicates the depth-averaged back-projected energy reduction we obtain for the ELB array. Dark and light grey rectangles indicate the 1- and 2-sigma intervals around the mean stack energy reduction for noise-only input using the ELB array geometry. Stars indicate the energy reduction computed for the 5 NIF earthquakes shown in Figure 2. b. The distribution of source depth error.

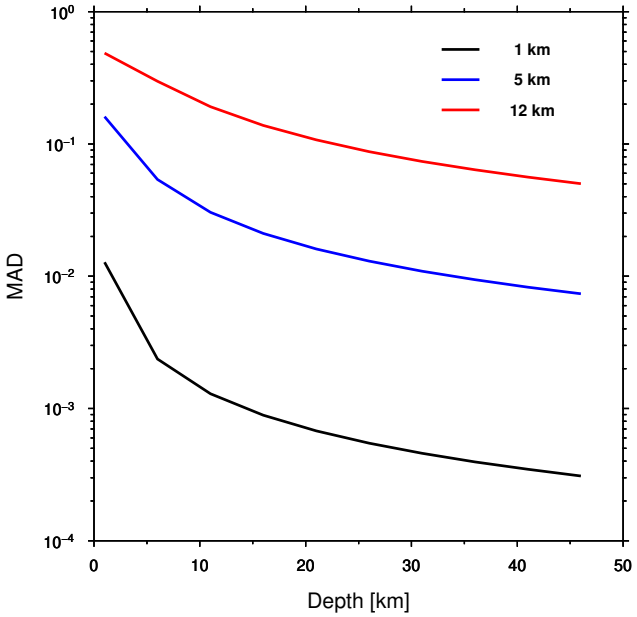

Figure 4. The median absolute deviation of the inter-array time delays as a function of the source depth. Black, blue, and red curves are for 1, 5, and 12 km array apertures, respectively. Travel times are calculated assuming a uniform velocity equal to 3.5 km/s.

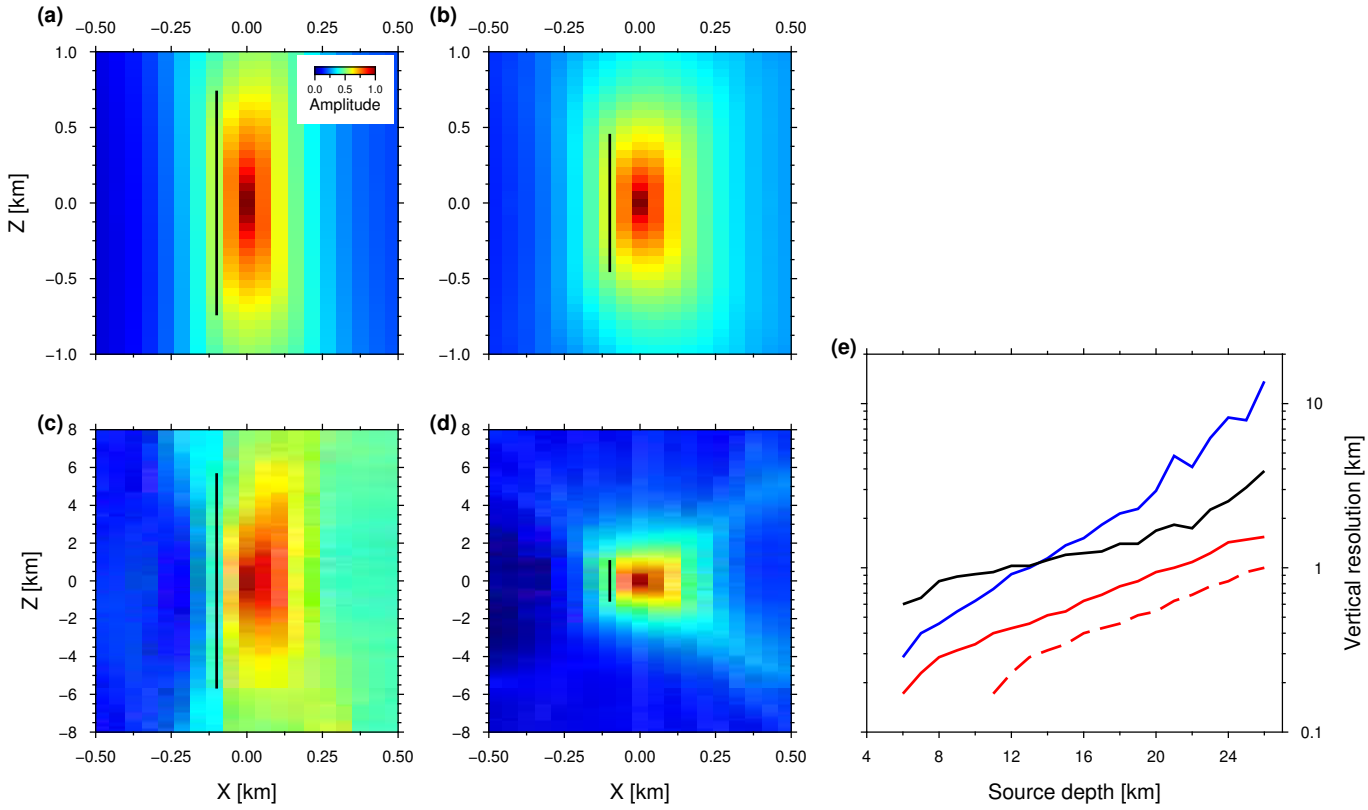

Figure 5. Resolution analysis. a-d. Point spread functions computed for an input source located at depth of 10 km (panels a,b) and 20 km (panels c,d). Vertical lines indicate the vertical resolution, defined as the length scale over which the resolution power decreases down to 80% of the maximum. a,c. ELB array. b,d. LB array. e. The vertical resolution scale as a function of source depth. Blue and red solid curves are for the ELB and LB array, respectively. Dashed red curve indicates the LB array vertical resolution after downward continuation. Black solid curve indicates the vertical resolution obtained using 1% of the LB array sensors.

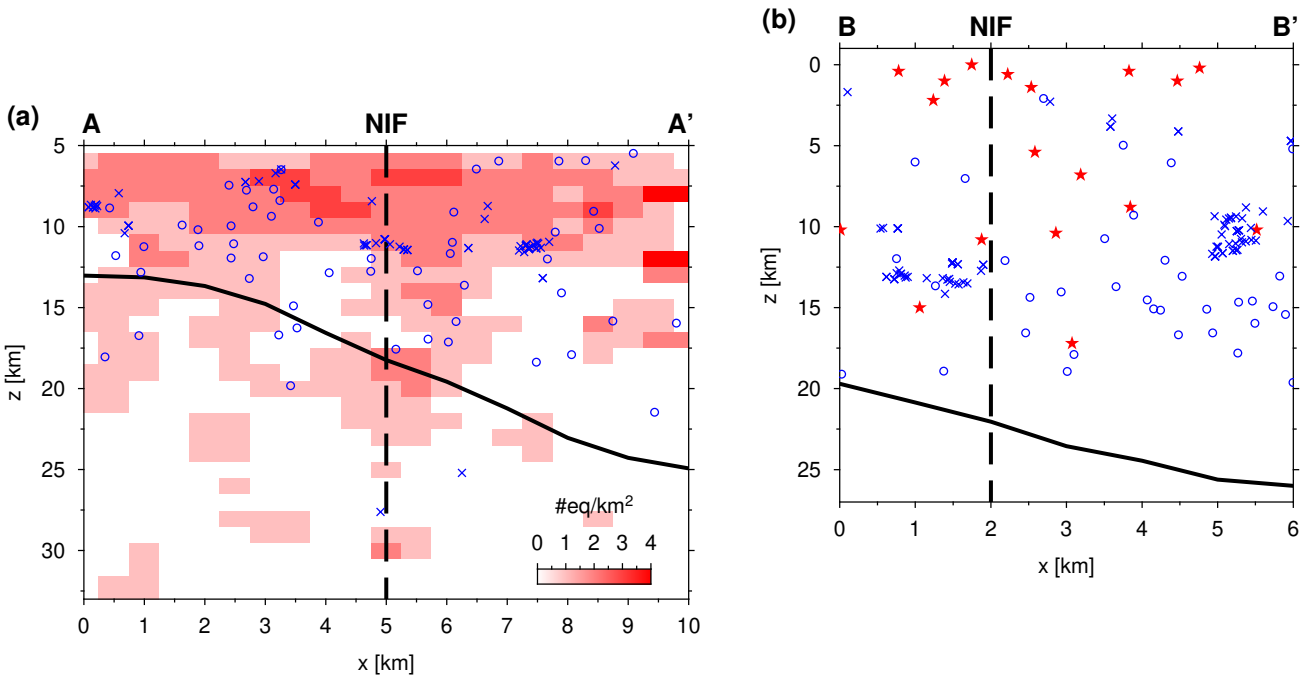

Figure 6. LB seismicity and Moho depth cross-sections. Earthquake densities from the LB array [*Inbal et al.*, 2016] are shown in shades of red. Blue circles and crosses indicate earthquake locations found in the regional Southern California Earthquake Center seismicity catalog, and in the match-filter-based catalog of *Ross et al.* [2019], respectively. Solid and dashed curves are for the Moho depth [*Clayton*, 2020], and the Newport-Inglewood fault, respectively. Red stars in panel b are for the locations in *Yang et al.* [2021]'s ELB catalog. The location of the cross-sections are shown in Figure 1. a. LB cross-section. b. ELB cross-section.